Japan Sea Thermohaline Structure and Circulation. Part II: A Variational P-Vector Method

PETER C. CHU, JIAN LAN, AND CHENWU FAN

Department of Oceanography, Naval Postgraduate School, Monterey, California

(Manuscript received 11 August 2000, in final form 30 January 2001)

ABSTRACT

The second part of this work investigates the seasonal variabilities of the Japan/East Sea (JES) circulation using the U.S. Navy Generalized Digital Environmental Model (GDEM) climatological temperature and salinity dataset (public domain) on a 0.5° × 0.5° grid. A variational P-vector method was developed to invert the velocity field. The GDEM for the JES was built up on historical (1930–97) 136 509 temperature and 52 572 salinity profiles. The climatological mean and seasonal variability of the current systems are well inverted, especially the Tsushima Warm Current and its bifurcation, the East Korean Warm Current (EKWC), the Japan nearshore branch, the confluence of the EKWC, and the North Korean Cold Current near the Korean coast and flows northeastward along the subpolar front, and a mesoscale anticyclonic eddy in the Ulleng/Tsushima Basin. Furthermore, this method has the capability to invert flow reasonably well across the shallow straits such as the Tsushima/Korea, Tsugaru, and Soya Straits. The GDEM temperature and salinity and the inverted velocity fields provide balanced initial fields for JES numerical modeling and simulation.

1. Introduction

The Japan Sea, known as the East Sea in Korea, has a steep bottom topography (Fig. 1) that makes it a unique semi-enclosed ocean basin overlaid by a pronounced monsoon surface wind. The Japan/East Sea (JES) covers an area of 10^6 km^2, has a maximum depth in excess of 3700 m, and is isolated from open oceans except for small (narrow and shallow) straits that connect the JES to the Pacific Ocean. The JES contains three major basins called the Japan Basin (JB), Ulleng/Tsushima Basin (UTB), and Yamato Basin (YB), and a high central seamount called the Yamato Rise (YR). The JES has a great scientific interest as a miniature prototype ocean. Its basinwide circulation pattern, boundary currents, Subpolar Front (SPF), mesoscale eddy activities and deep water formation are similar to those in a large ocean.

The JES experiences two monsoons, winter and summer, every year. During the winter monsoon season, a cold northwest wind blows over the JES as a result of the Siberian High Pressure System located over the East Asian continent. Radiative cooling and persistent cold air advection maintain cold air over the JES. The northwest–southeast oriented jet stream is positioned at the JES. A typical winter monsoon pattern lasts nearly six months (Nov to Apr). During the summer monsoon, a warm and weaker southeast wind blows over the JES. A typical summer monsoon pattern lasts nearly four months (mid-May to mid-Sep).

The JES general circulation has been investigated for several decades. The Tsushima Warm Current (TWC), dominating the surface layer, flows in from the Tsushima Strait, and carries warm water from the south up to 40°N where a polar front forms (Seung and Yoon 1995). Most of the nearly homogeneous water in the deep part of the basin is called the Japan Sea Proper Water (Moriyasu 1972) and is of low temperature and low salinity. Above the proper water, warm and saline water that enters through the Tsushima Strait flows northeastward and flows out through the Tsugaru and Soya Straits.

The TWC separates north of 35°N into western and eastern channels (Uda 1934; Kawabe 1982a,b; Chu et al. 2001a; Chu et al. 2001b). The flow through the western channel closely follows the Korean coast [called the East Korean Warm Current (EKWC)] until it bifurcates into two branches near 37°N. The eastern branch follows the SPF to the western coast of Hokkaido Island, and the western branch moves northward and forms a cyclonic eddy at the Eastern Korean Bay (EKB). The flow through the eastern channel follows the Japanese coast, called the "Nearshore Branch" by Yoon (1982). More accurately, we may call it the Japan nearshore branch (JNB). The JNB is usually weaker than the EKWC. The TWC at both channels reduces with depth. The North Korea Cold Current (NKCC) meets the EKWC at about 38°N with some seasonal meridional migration. After separation from the coast, the NKCC and the EKWC

Corresponding author address: Dr. Peter C. Chu, Dept. of Oceanography, Naval Postgraduate School, Monterey, CA 93943.
E-mail: chu@nps.navy.mil

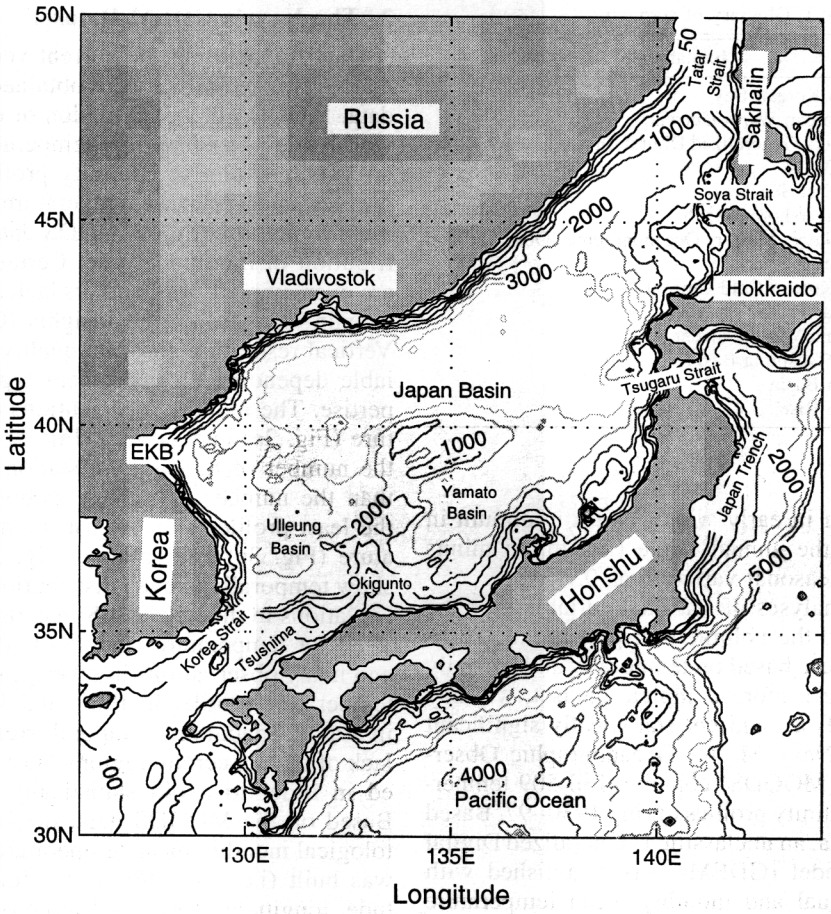

FIG. 1. Geography and isobaths showing the bottom topography of the Japan/East Sea (JES).

converge and form a strong front (i.e., SPF) that stretches in a west–east direction across the basin. The NKCC makes a cyclonic recirculation gyre in the north, but most of the EKWC flows out through the outlets (Uda 1934). The formation of NKCC and the separation of EKWC are due to a local forcing by wind and buoyancy flux (Seung 1992). Large meanders develop along the front and are associated with warm and cold eddies.

The seasonal variability of the TWC at the Tsushima/Korea Strait largely impacts the JES physical conditions. An accurate estimate of the volume transport at this strait is important for the JES circulation and thermohaline structure. Two methods have been used to estimate the volume transport through the Tsushima/Korea Strait: 1) dynamical calculation of the hydrographic data with a level of "no motion" at the bottom and 2) calculation of the sea level difference across the strait.

Using the dynamical calculation approach, the volume transport through the Tsushima/Korea Strait is characterized by the minimum in winter–spring, and maximum in summer–fall (e.g., Hidaka and Suzuki 1950; Yi 1966). For example, Yi (1966) estimated the annual average of 1.3 Sv, a maximum of 2.2 Sv in October, and a minimum of 0.3 Sv in February (Sv $\equiv 10^6$ m^3 s^{-1}). Later on, Mitta and Ogawa (1984) analyzed the historical velocity data obtained by the current measurements lasting one day in the summers of 1942 and 1943 to investigate the current structure across the Tsushima/Korea Strait. The data show intense northward currents near the bottom in the Tsushima/Korea Strait. This leads to doubt about the validity of the dynamical calculation with the level of no motion at the bottom of the strait (Mitta and Ogawa 1984). To remove the "level of no motion" assumption, we use an inverse method to obtain absolute geostrophic velocity from hydrographic data.

Using the sea level difference across the strait without considering the contribution from baroclinic motion, Kawabe (1982a) and Toba et al. (1982) found the volume transport through the Tsushima/Korea Strait to be the same as the dynamical calculation (Hidaka and Suzuki 1950; Yi 1966). Considering the effect of baroclinic motion and subtracting the sea level difference due to the baroclinic motion from the observed current data (1988–90), Isobe (1994) found that the volume transport

TABLE 1. Glossary of acronyms.

Acronym	Explanation
EKB	Eastern Korean Bay
EKWC	East Korean Warm Current
GDEM	U.S. Navy Generalized Digital Environmental Model
JB	Japan Basin
JES	Japan/East Sea
JNB	Japan nearshore branch
MOODS	U.S. Navy Master Oceanographic Observational Data Set
NKCC	North Korean Cold Current
SPF	Subpolar Front
TWC	Tsushima Warm Current
UTB	Ulleng/Tsushima Basin
YB	Yamato Basin
YR	Yamato Rise

was at a maximum in early winter and a minimum in early spring with the annual range (maximum minus minimum) of the seasonal variation as 0.7 Sv.

Most of these analyses of seasonal variability of the JES circulation and the volume transport at the Tsushima/Korea Strait were based on temporally and spatially limited data. Using a more complete dataset, we may improve these analyses and get statistically significant results. The U.S. Navy Master Oceanographic Observational Data Set (MOODS) contains 136 509 temperature and 52 572 salinity profiles during 1930–97. Based on the MOODS data, an unclassified Generalized Digital Environmental Model (GDEM) was established with climatological annual and monthly mean temperature and salinity fields on a 0.5° × 0.5° grid.

Chu et al. (2001a) used the P-vector inverse method (Chu 1995, 2000; Chu et al. 1998a,b) to calculate the JES absolute geostrophic velocity from the GDEM data. The P-vector method contains two steps: 1) determination of the velocity direction and 2) determination of the velocity magnitude. Two necessary conditions for the inversion are easily implemented into this method: 1) the isopycnal surface does not parallel the isosurface of potential vorticity and 2) the velocity has a vertical spiral (Chu et al. 1998a,b). The P-vector method inverts the circulation in the JES basin reasonably well (Chu et al. 2001a), but it fails to invert the velocity field at shallow straits such as the Tsushima/Korea, Tsugaru, and Soya Straits.

In this study, we develop a variational P-vector method to improve the inversion and to obtain realistic circulation in the JES basin as well as in the shallow straits. The outline of this paper is as follows. A description of the GDEM data is given in section 2. The P-vector method and its deficiencies are presented in section 3. The variational P vector is presented in section 4. The inverted absolute geostrophic velocity field is discussed in section 5. The volume transports in the Tsushima/Korea, Tsugaru, and Soya Straits are presented in section 6. In section 7 we present our conclusions. There are quite a few acronyms used in this paper, listed in Table 1.

2. The Navy's GDEM Dataset

Data for building the current version of GDEM climatology for the JES were obtained from the MOODS data. MOODS is a compilation of ocean data observed worldwide consisting of 1) temperature-only profiles, 2) both temperature and salinity profiles, 3) sound-speed profiles, and 4) surface temperature (drifting buoy). The main limitation of the MOODS data is its irregular distribution in time and space. Certain periods and areas are oversampled, while others lack enough observations to gain any meaningful insights (Chu et al. 1997a,b). Vertical resolution and data quality are also highly variable depending on instrument type and sampling expertise. The monthly distributions of the JES temperature (Fig. 2a) and salinity (Fig. 2b) stations show that the number of temperature stations is 2–3 times more than the number of salinity stations, and January has the least profiles and August the most. Yearly temperature (Fig. 3a) and salinity (Fig. 3b) profile numbers show temporally uneven distribution with almost no observations in the whole JES in certain years (e.g., 1944, 1989 for temperature, and 1944, 1987–93 for salinity) and many observations in other years (e.g., nearly 6500 temperature profiles in 1969, and 3700 salinity profiles in 1967). Spatial and temporal irregularities along with lack of data in certain regions must be carefully weighted in order to avoid statistically induced variability. Based on the MOODS data, the Navy's global climatological monthly mean temperature and salinity dataset was built (i.e., GDEM) with a four-dimensional (latitude, longitude, depth, and month) display.

The basic design concept of GDEM is the determination of a set of analytical curves that represent the mean vertical distributions of temperature and salinity for grid cells (0.5° × 0.5°) through the averaging of the coefficients for the curves found for individual profiles (Teague et al. 1990). Different families of representative curves have been chosen for shallow, middepth, and deep-depth ranges, with each chosen so that the number of parameters required to yield a smooth, mean profile over the range was minimized. As pointed out by Teague et al. (1990), large-scale oceanographic features are generally found to be similarly represented in both GDEM and the NOAA *Climatological Atlas of the World Ocean* temperature and salinity. GDEM appears to render better representations of seasonal variability and regions of high current shear because of a different smoothing method and a finer grid spacing. GDEM data contains the monthly mean temperature and salinity (T, S) and annual mean temperature and salinity ($\bar{T}$, $\bar{S}$) fields. Interested readers are referred to Teague et al. (1990) for more information.

3. P-vector inverse method and its deficiency

a. Reduced physics

As pointed out by Wunsch and Grant (1982), in determining large-scale circulation from hydrographic

data, we can be reasonably confident of the assumptions of geostrophic balance, mass conservation, adiabatic, and no major cross-isopycnal mixing (except for water masses in contact with the atmosphere). Under these conditions, the density of each fluid element would be conserved, which mathematically is given by

$$\mathbf{V} \cdot \nabla\rho = 0, \tag{1}$$

where ρ is the potential density and $\mathbf{V} = (u, v, w)$ is the geostrophic velocity. The conservation of potential vorticity equation can be obtained by differentiating (1) with respect to z, using geostrophic and hydrostatic balances, and including the latitudinal variation of the Coriolis parameter to give

$$\mathbf{V} \cdot \nabla q = 0, \tag{2}$$

where $q = f\partial\rho/\partial z$. Equations (1) and (2) imply that the velocity $\mathbf{V}$ is parallel to $\nabla q \times \nabla\rho$.

b. Necessary conditions

Stommel and Schott (1977) pointed out that the three-dimensional velocity field cannot be determined from the density field alone when the q and ρ surfaces coincide. The first necessary condition for the validity of this inverse method is as follows.

Condition 1: The ρ surface is not parallel to the q surface, which mathematically requires

$$\nabla\rho \times \nabla q \neq 0.$$

Stommel and Schott (1977) further pointed out that the three-dimensional velocity field cannot be determined from the ρ field alone if the horizontal velocity does not rotate with depth (β spiral). The existence of the β spiral is the second necessary condition.

Condition 2: The velocity (u, v) should execute a β spiral, which mathematically requires that, for at least two depths, $z = z_k$ and $z = z_m$, with horizontal velocities $[u^{(k)}, v^{(k)}]$ and $[u^{(m)}, v^{(m)}]$,

$$\begin{vmatrix} u^{(k)} & v^{(k)} \\ u^{(m)} & v^{(m)} \end{vmatrix} \neq 0.$$

If we cannot find levels z_k and z_m such that the necessary condition 2 is satisfied, the inverse method will fail to get velocity in that water column.

c. P-vector method

Consider the unit vector $\mathbf{P}$ (Chu 1995), defined by

$$\mathbf{P} = \frac{\nabla\rho \times \nabla q}{|\nabla\rho \times \nabla q|}. \tag{3}$$

The existence of this unit vector implies nonzero denominator of (3), which is the necessary condition 1.

The velocity, $\mathbf{V} = (u, v, w)$, parallels the unit vector $\mathbf{P}$,

$$\mathbf{V} = r(x, y, z)\mathbf{P}, \tag{4}$$

where r is the proportionality. Applying the thermal wind relation at two different depths z_k and z_m, a set of algebraic equations for determining the parameter r is obtained:

$$\begin{aligned} r^{(k)}P_x^{(k)} - r^{(m)}P_x^{(m)} &= \Delta u_{km} \\ r^{(k)}P_y^{(k)} - r^{(m)}P_y^{(m)} &= \Delta v_{km}, \end{aligned} \tag{5}$$

which are two linear algebraic equations for $r^{(k)}$ and $r^{(m)}$ $[r^{(i)} = r(x, y, z_i)]$. Here

$$(\Delta u_{km}, \Delta v_{km}) = \frac{g}{f\rho_0}\int_{z_m}^{z_k}\left(\frac{\partial\hat{\rho}}{\partial y}, -\frac{\partial\hat{\rho}}{\partial x}\right)dz, \tag{6}$$

where $\hat{\rho}$ is the in situ water density, and ρ_0 is the characteristic value of the density.

The existence of a solution of (5) implies a nonzero determinant of the coefficient matrix of (5), which is necessary condition 2. This determinant is the sine of the vertical turning angle between $\mathbf{P}_h^{(k)}$ and $\mathbf{P}_h^{(m)}$ (Chu 2000; Chu et al. 1998a,b; 2001a).

For water columns satisfying the two necessary conditions, we solve (6) to obtain $r^{(k)}$ for the level z_k. There are $N - 1$ sets ($m = 1, 2, k - 1, k + 1, \cdots, N$) of equations (5) for calculating $r^{(k)}$. Here N is the total number of vertical levels of the water column. The $N - 1$ sets of equations are compatible under the thermal wind constraint and should provide the same solution. However, because of errors in measurements (instrumentation errors) and computations (truncation errors), the parameters $r^{(k)}$ may vary with m. A least squares error algorithm is used to minimize the error.

d. Deficiency of the current P-vector method

Let $(u^{(P)}, v^{(P)})$ be the absolute velocity determined by the P-vector method, and $(U^{(P)}, V^{(P)})$ be their vertical integrations,

$$(U^{(P)}, V^{(P)}) = \int_{-H}^{0}(u^{(P)}, v^{(P)})\,dz. \tag{7}$$

Due to the local determination of the absolute geostrophic velocity, the present P-vector method does not always guarantee mass conservation over a domain σ, that is,

$$\iint_\sigma\left[\frac{\partial U^{(P)}}{\partial x} + \frac{\partial V^{(P)}}{\partial y}\right]dx\,dy \neq 0 \tag{8}$$

is possible. Such a deficiency largely affects the quality of the inversion. For example, the TWC in the shallow Tsushima/Korea Strait was not well inverted (Chu et al. 2001a). Therefore, we develop a variational algorithm taking into account the mass conservation.

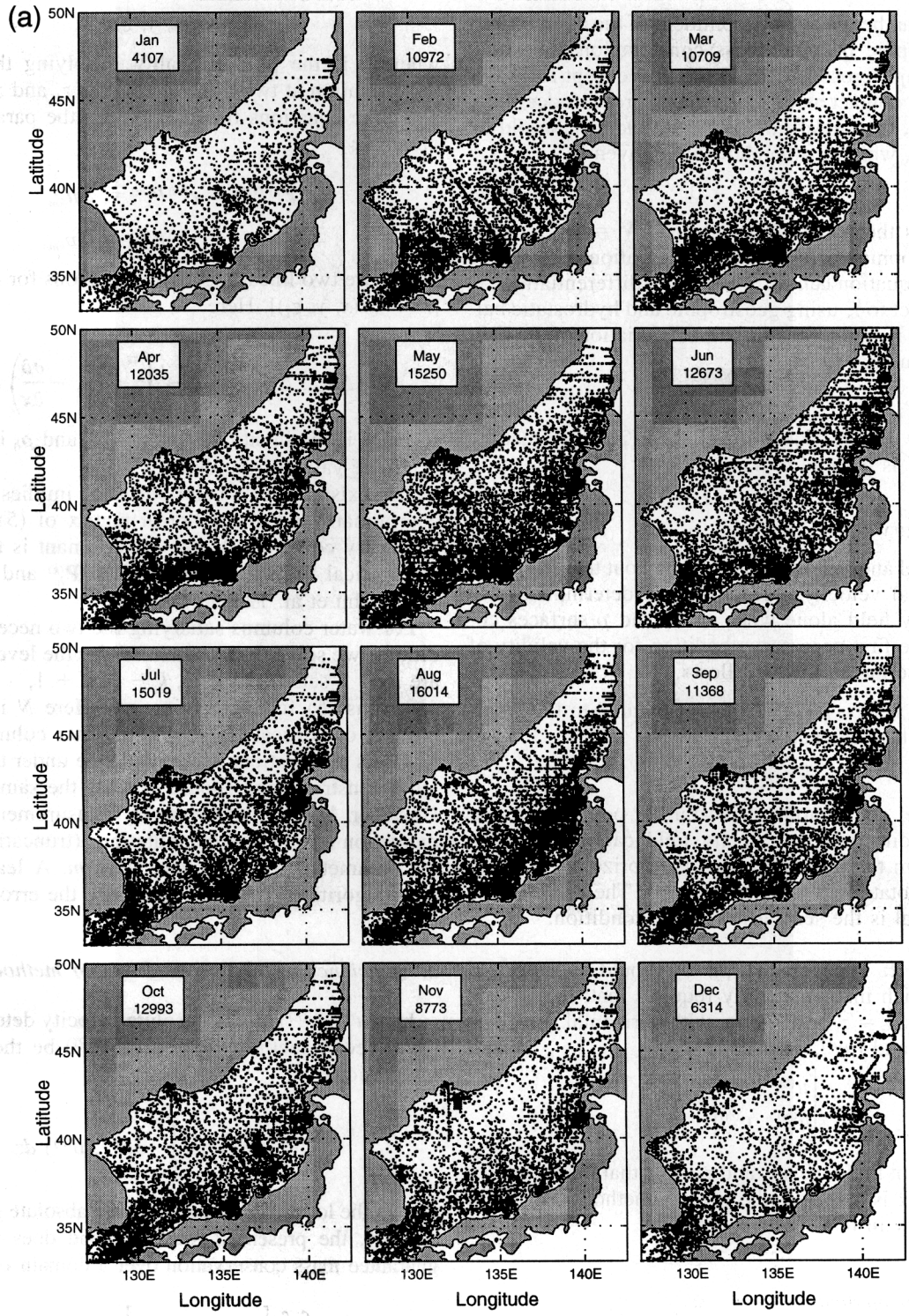

FIG. 2. Spatial distributions of MOODS stations during 1930–97: (a) temperature and (b) salinity.

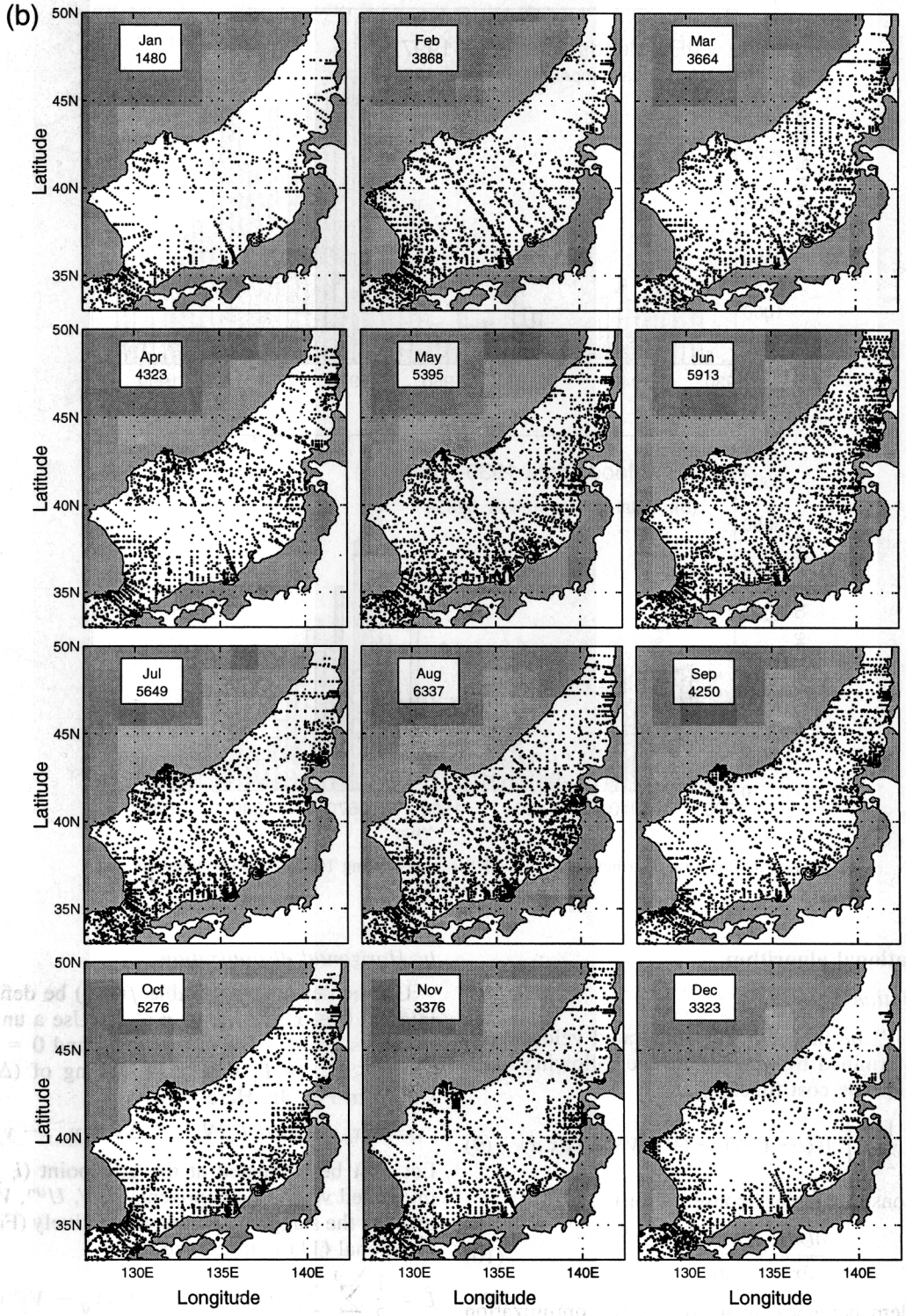

FIG. 2. (*Continued*)

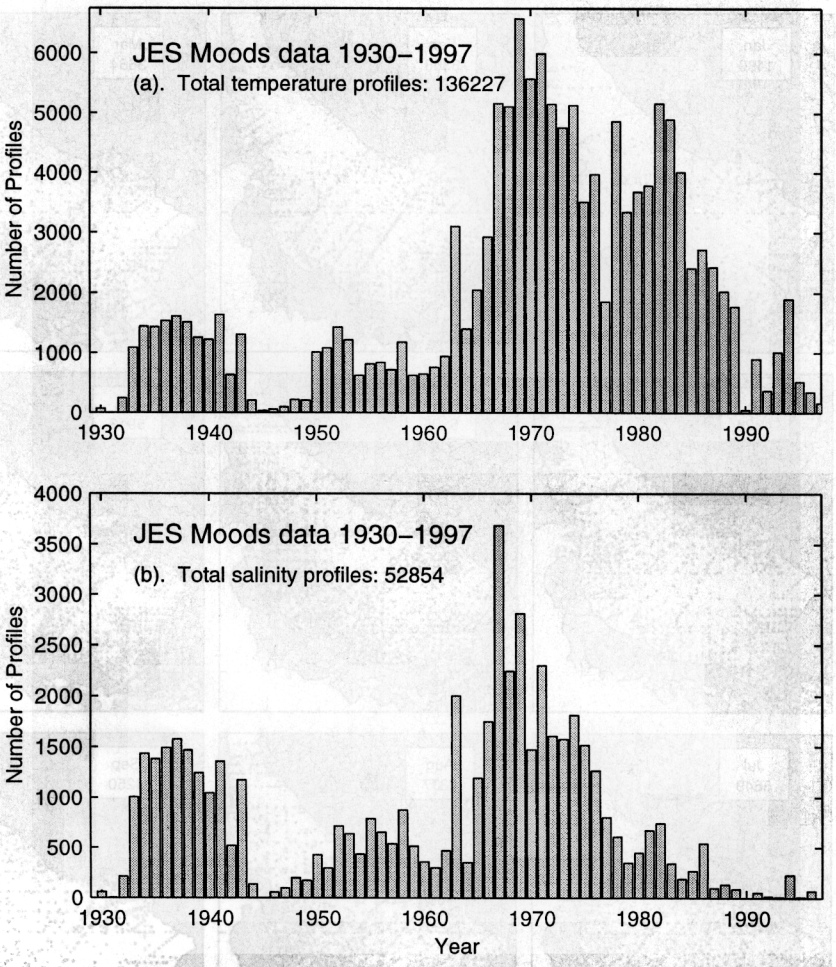

FIG. 3. Temporal distributions of MOODS stations during 1930–97: (a) temperature and (b) salinity.

4. A variational algorithm

a. Formulation

Let (U, V) be the vertically integrated velocity optimally determined by minimizing the following functional (called the cost function),

$$J(U, V) = \frac{1}{2}\iint_{\sigma} [(U - U^{(P)})^2 + (V - V^{(P)})^2]\, dx\, dy \quad (9)$$

with the constraint (mass conservation)

$$\frac{\partial U^{(P)}}{\partial x} + \frac{\partial V^{(P)}}{\partial y} = 0. \quad (10)$$

This problem becomes an unconstrained optimization using

$$L(U, V, \lambda) = J(U, V) + \iint_{\sigma} \lambda \left[\frac{\partial U^{(P)}}{\partial x} + \frac{\partial V^{(P)}}{\partial y}\right] dx\, dy, \quad (11)$$

where λ is the Lagrangian parameter.

b. Horizontal discretization

Let the dependent variable $f(x, y)$ be defined on the interval $0 \le x \le L_x$, $0 \le y \le L_y$. Use a uniform grid, $0 = x_1 < x_2 < \cdots < x_{N_x} = L_x$, and $0 = y_1 < y_2 < \cdots < y_{N_y} = L_y$ with grid spacing of $(\Delta x, \Delta y)$, as shown in Fig. 4a. Here,

$$\Delta x = x_{i+1} - x_i = L_x/N_x, \qquad \Delta y = y_{j+1} - y_j = L_y/N_y.$$

Let ρ, λ be evaluated at the grid point (i, j), and the integrated velocity components U, V, $U^{(P)}$, $V^{(P)}$ be evaluated at the staggered points, respectively (Fig. 4b). The functional (11) is discretized as

$$\begin{aligned}\hat{L} = {} & \frac{1}{2}\sum_{i=1}^{N_x-1}\sum_{j=1}^{N_y-1} [(U_{ij} - U_{ij}^{(P)})^2 + (V_{ij} - V_{ij}^{(P)})^2]\Delta x \Delta y \\ & + \frac{1}{2}\sum_{i=1}^{N_x-1}\sum_{j=1}^{N_y-1} \lambda_{ij}(U_{ij} + U_{i,j-1} - U_{i-1,j} - U_{i-1,j-1})\Delta y \\ & + \frac{1}{2}\sum_{i=1}^{N_x-1}\sum_{j=1}^{N_y-1} \lambda_{ij}(V_{ij} + V_{i-1,j} - V_{i,j-1} - V_{i-1,j-1})\Delta x. \end{aligned} \quad (12)$$

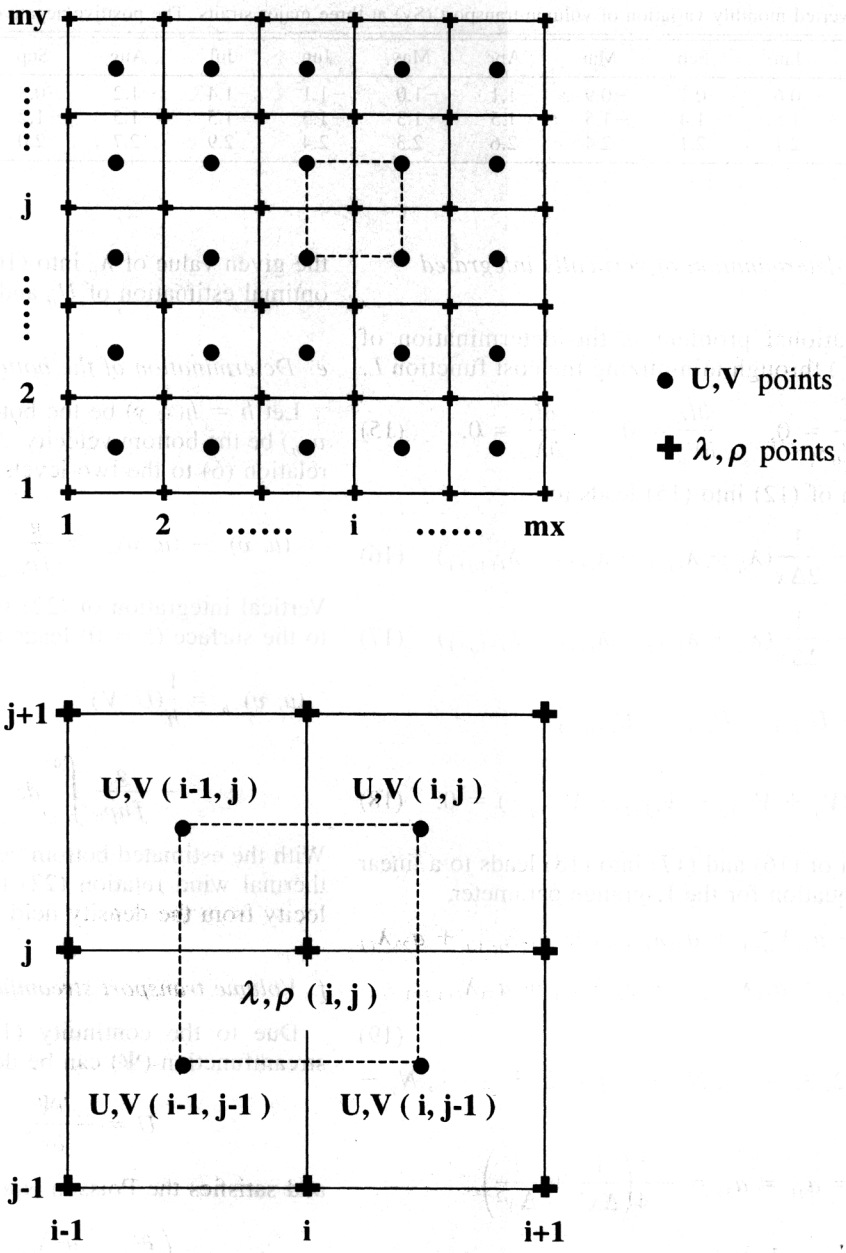

FIG. 4. Staggered grid used for the computation: (a) grid distribution and (b) staggered grids for (u, v) and standard grids for (λ, ρ).

c. Combined local–global determination

Minimization of $\hat{L}$ becomes a combination of local determination at the staggered grid (i, j) for velocity (β-spiral approach)

$$U_{ij} \rightarrow U_{ij}^{(P)}, \qquad V_{ij} \rightarrow V_{ij}^{(P)} \tag{13}$$

and global determination (box model)

$$\frac{1}{\Delta x}(U_{ij} + U_{i,j-1} - U_{i-1,j} - U_{i-1,j-1}) + \frac{1}{\Delta y}(V_{ij} + V_{i-1,j} - V_{i,j-1} - V_{i-1,j-1}) \rightarrow 0, \tag{14}$$

which keeps the mass conservation at any box centered at the nonstaggered grid for ρ and λ (Fig. 4b). Thus, this variational P-vector method can be treated as a β-spiral box model.

TABLE 2. Inverted monthly variation of volume transport (Sv) at three major straits. The positive/negative values mean inflow/outflow.

	Jan	Feb	Mar	Apr	May	Jun	Jul	Aug	Sep	Oct	Nov	Dec
Soya	−0.6	−0.7	−0.9	−1.1	−1.0	−1.1	−1.4	−1.2	−0.8	−0.7	−0.5	−0.5
Tsugaru	−1.5	−1.4	−1.5	−1.5	−1.3	−1.3	−1.5	−1.5	−1.2	−1.5	−1.4	−1.6
Tsushima	2.1	2.1	2.4	2.6	2.3	2.4	2.9	2.7	2.0	2.2	1.9	2.1

d. Optimal determination of vertically integrated velocity

The variational problem is the determination of $(U_{ij}, V_{ij}, \lambda_{ij})$ through minimizing the cost function L,

$$\frac{\partial \hat{L}}{\partial U_{ij}} = 0, \qquad \frac{\partial \hat{L}}{\partial V_{ij}} = 0, \qquad \frac{\partial \hat{L}}{\partial \lambda_{ij}} = 0. \tag{15}$$

Substitution of (12) into (15) leads to

$$U_{ij} = U_{ij}^{(P)} - \frac{1}{2\Delta x}(\lambda_{ij} + \lambda_{i,j+1} - \lambda_{i+1,j} - \lambda_{i+1,j+1}) \tag{16}$$

$$V_{ij} = V_{ij}^{(P)} - \frac{1}{2\Delta y}(\lambda_{ij} + \lambda_{i+1,j} - \lambda_{i,j+1} - \lambda_{i+1,j+1}) \tag{17}$$

$$\frac{1}{\Delta x}(U_{ij} + U_{i,j-1} - U_{i-1,j} - U_{i-1,j-1}) + \frac{1}{\Delta y}(V_{ij} + V_{i-1,j} - V_{i,j-1} - V_{i-1,j-1}) = 0. \tag{18}$$

Substitution of (16) and (17) into (18) leads to a linear algebraic equation for the Lagrange parameter,

$$a_{11}\lambda_{i-1,j-1} + a_{21}\lambda_{i,j-1} + a_{31}\lambda_{i+1,j-1} + a_{12}\lambda_{i-1,j} + a_{22}\lambda_{i,j} + a_{32}\lambda_{i+1,j} + a_{13}\lambda_{i-1,j+1} + a_{23}\lambda_{i,j+1} + a_{33}\lambda_{i+1,j+1} = S_{ij}, \tag{19}$$

where $i = 2, 3, \cdots, N_x - 1$; $j = 2, 3, \cdots, N_y - 1$; and

$$a_{11} = a_{13} = a_{31} = a_{33} = -\frac{1}{4}\left(\frac{1}{\Delta x^2} + \frac{1}{\Delta y^2}\right),$$

$$a_{22} = \left(\frac{1}{\Delta x^2} + \frac{1}{\Delta y^2}\right),$$

$$a_{21} = a_{23} = -a_{12} = -a_{32} = \frac{1}{2}\left(\frac{1}{\Delta x^2} - \frac{1}{\Delta y^2}\right) \tag{20}$$

and

$$S_{ij} = \frac{1}{2\Delta x}(U_{ij}^{(P)} + U_{i,j-1}^{(P)} - U_{i-1,j}^{(P)} - U_{i-1,j-1}^{(P)}) + \frac{1}{2\Delta y}(V_{ij}^{(P)} + V_{i-1,j}^{(P)} - V_{i,j-1}^{(P)} - V_{i-1,j-1}^{(P)}). \tag{21}$$

The alternative direction implicit method (Press et al. 1986) is used to obtain the value of the Lagrange parameter at the grid point, λ_{ij}, solving (19). Substituting the given value of λ_{ij} into (16) and (17), we obtain the optimal estimation of U_{ij} and V_{ij}.

e. Determination of the bottom velocity

Let $h = h(x, y)$ be the bottom topography and (u_{-h}, v_{-h}) be the bottom velocity. Applying the thermal wind relation (6) to the two levels z and $-h$, we have

$$(u, v)_z - (u, v)_{-h} = \frac{g}{f\rho_0}\int_{-h}^{z}\left(\frac{\partial \hat{\rho}}{\partial y}, -\frac{\partial \hat{\rho}}{\partial x}\right)dz'. \tag{22}$$

Vertical integration of (22) from the bottom ($z = -h$) to the surface ($z = 0$) leads to

$$(u, v)_{-h} = \frac{1}{h}(U, V) - \frac{g}{fh\rho_0}\int_{-h}^{0} dz \int_{-h}^{z}\left(\frac{\partial \hat{\rho}}{\partial y}, -\frac{\partial \hat{\rho}}{\partial x}\right)dz'. \tag{23}$$

With the estimated bottom velocity $(u, v)_{-h}$, we use the thermal wind relation (22) to obtain the absolute velocity from the density field.

f. Volume transport streamfunction

Due to the continuity (10), the volume transport streamfunction (Ψ) can be defined by

$$U = -\frac{\partial \Psi}{\partial y}, \qquad V = \frac{\partial \Psi}{\partial x} \tag{24}$$

and satisfies the Poisson equation

$$\left(\frac{\partial^2}{\partial x^2} + \frac{\partial^2}{\partial y^2}\right)\Psi = \frac{\partial V}{\partial x} - \frac{\partial U}{\partial y}. \tag{25}$$

5. Absolute geostrophic velocity

a. Annual mean

Figure 5 shows the inverted horizontal velocity vectors at depths 0, 50, 100, 150, 200, and 300 m respectively. The variational P-vector method inverts the velocity well at the three major straits: Tsushima/Korea, Tsugaru, and Soya Straits. However, the flow in Tatar Strait is not well resolved due to the poor data quality.

We take the velocity field at depths 0, 50, and 100 m (150, 200, and 300 m) to represent the upper (intermediate)-layer circulation features. The inverted flow

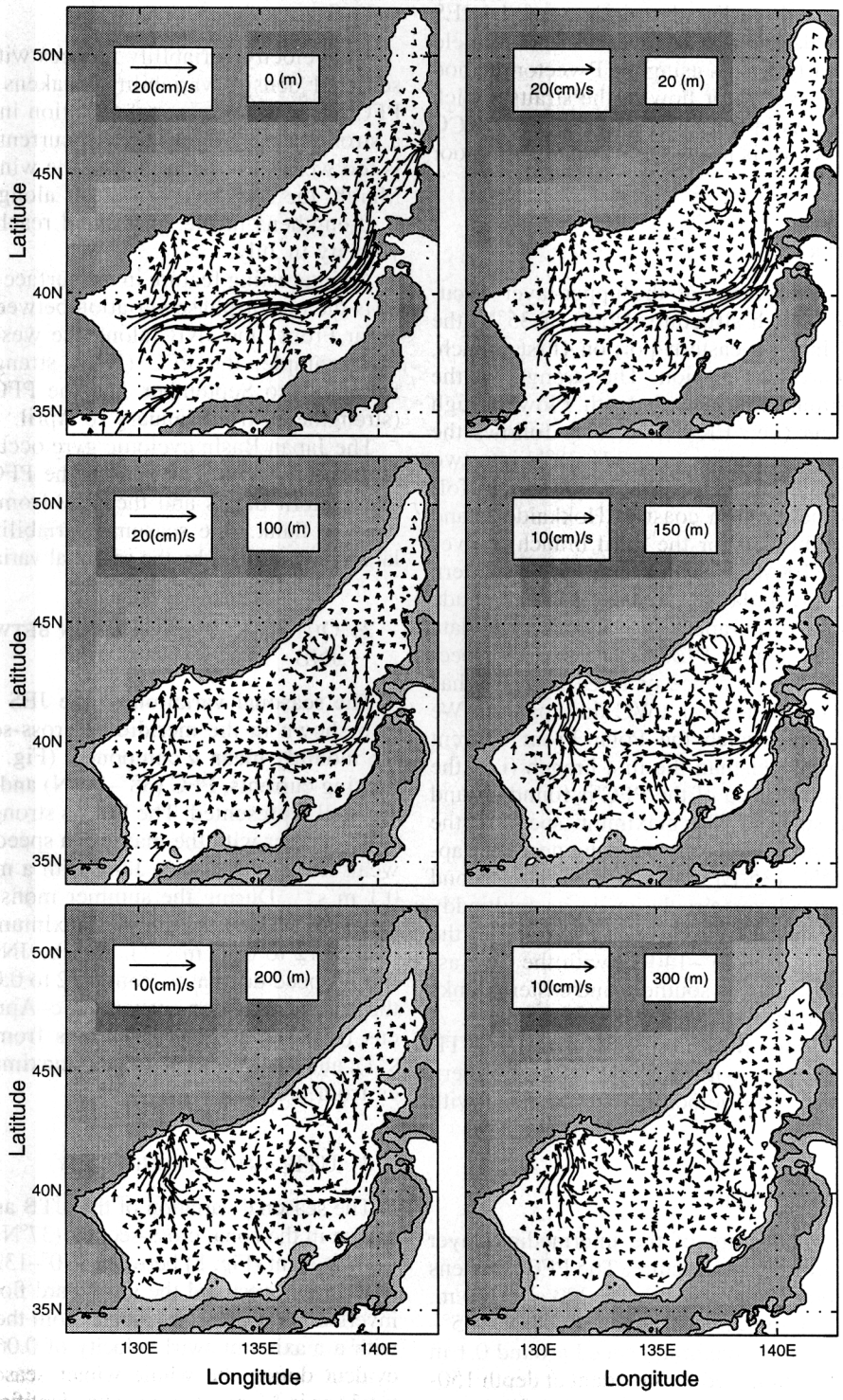

FIG. 5. Inverted annual mean horizontal velocity vectors at different depths: (a) 0, (b) 50 m, (c) 100 m, (d) 150 m, (e) 200 m, and (f) 300 m.

pattern coincides with earlier descriptions of the JES circulation (e.g., Uda 1934). The inverted velocity field agrees well with early results using the P-vector method (Chu et al. 2001a) except for flow in the straits, which is much improved. As in Chu et al. (2001a), the NKCC along the Russian coast is not well inverted due to poor data quality.

1) Upper layer

The most striking feature of the upper-layer circulation is its three-branch structure. North of 35°N, the TWC bifurcates into an eastern portion (first branch, i.e., JNB) and a western portion. The strength of the TWC at both portions reduces with depth. Flow through the western portion (i.e., EKWC) closely follows the Korean coast until it separates near 37°–38°N into two branches: the offshore branch (the second branch) follows the SPF to the western coast of Hokkaido Island and the longshore branch (or the third branch) moves northward (i.e., the EKWC). Such a three-branch pattern was first identified by Suda and Hidaka (1932) and Suda et al. (1932) using hydrographic and current meter data from June to September in 1929 and in 1930, respectively. Since then, the existence of three branches has been believed to be the typical TWC flow pattern. We may call the second branch the Polar Front Current (PFC), which is stronger than the first branch (i.e., the JNB). The maximum speed of the PFC is found around 0.2 m s^{-1} at the surface. The maximum speed of the JNB is found around 0.1 m s^{-1}, occurring near the Japanese coast (35.5°N, 135°E) at the surface. The second feature of the upper-layer circulation is its multieddy structure. An evident cyclonic gyre is identified in the Japan Basin (38°–44°N, 135°–140°E) with the flow associating with the PFC as its southern and eastern flanks and the flow from the north as its western flank. A mesoscale anticyclonic eddy is identified in the UTB (36°–38°N, 130°–132°E) with the PFC as its northern and western flanks. The velocity field weakens with depth.

2) Intermediate layer

The most striking feature of the intermediate-layer circulation is its multieddy structure. The PFC weakens at depth 150 m and disappears at depth 200 and 300 m. The cyclonic gyre in the Japan Basin (38°–44°N, 135°–140°E) is evident with a maximum speed around 0.1 m s^{-1}. The UTB anticyclonic eddy is evident at depth 150- and 200-m depth and weakens drastically at 300 m.

b. Seasonal variability

The seasonal variability of the inverted absolute geostrophic velocity (not in the straits) is quite similar to an early study using the ordinary P-vector method (Chu et al. 2001a).

1) Surface circulation

The velocity variability reduces with depth since the seasonal density variability weakens with depth. The PFC has a weak seasonal variation in flow pattern and a strong seasonal variation in current speed. The JNB is too weak to be identified in the winter (Dec–Feb). In March, the JNB starts to occur along the Japan coast. It strengthens in the spring and reaches the maximum velocity in July.

An interesting feature in the surface current field (Fig. 6) is the out-of-phase variation between PFC (along the Polar Front) and JNB (along the west coast of Japan). For example, the PFC (JNB) strengthens (weakens) from July to September, and the PFC (JNB) weakens (strengthens) from January to April.

The Japan Basin cyclonic gyre occurs all year round, with the flow associated with the PFC as the southern and eastern flanks and the flow from the north as the western flank. The seasonal variability of this gyre is largely determined by the seasonal variability of the PFC.

2) Out-of-phase variation between PFC and JNB

The seasonal variation of the JES major currents is also shown in the meridional cross-section (135°E) of the monthly mean u component (Fig. 7). Two eastward flowing currents, PFC (38°–40°N) and JNB (36°–37°N), are well represented. The PFC is strong from September to December with the maximum speed of 0.2 m s^{-1} and weak from February to June with a minimum speed of 0.1 m s^{-1}. During the summer monsoon season (Jun–Oct), the PFC strengthens (maximum speed increases from 0.12 to 0.18 m s^{-1}), and the JNB weakens (maximum speed decreases from 0.12 to 0.04 m s^{-1}). During the winter monsoon season (Dec–Apr), the PFC weakens (maximum speed decreases from 0.18 to 0.12 m s^{-1}), and the JNB strengthens (maximum speed increases from 0.04 to 0.12 m s^{-1}).

3) UTB anticyclonic eddy

The seasonal variation of the UTB anticyclonic eddy is shown in the zonal cross-section (37°N) of monthly mean v component (Fig. 8) between 130°–132°E: the northward flow in the west and the southward flow in the east. The inverted UTB eddy has a core from the surface to 100-m with a maximum swirl velocity of 0.06 m s^{-1}. It is quite evident during the whole winter season (Dec–Feb) and weakens in March. It cannot be identified at the 37°N cross section from spring to early summer (Apr–Jun) and becomes evident again in late summer (Aug).

4) Flow through the Tsushima/Korea Strait

The monthly mean surface velocity vector field in Tsushima/Korea Strait (Fig. 9) shows the capability of

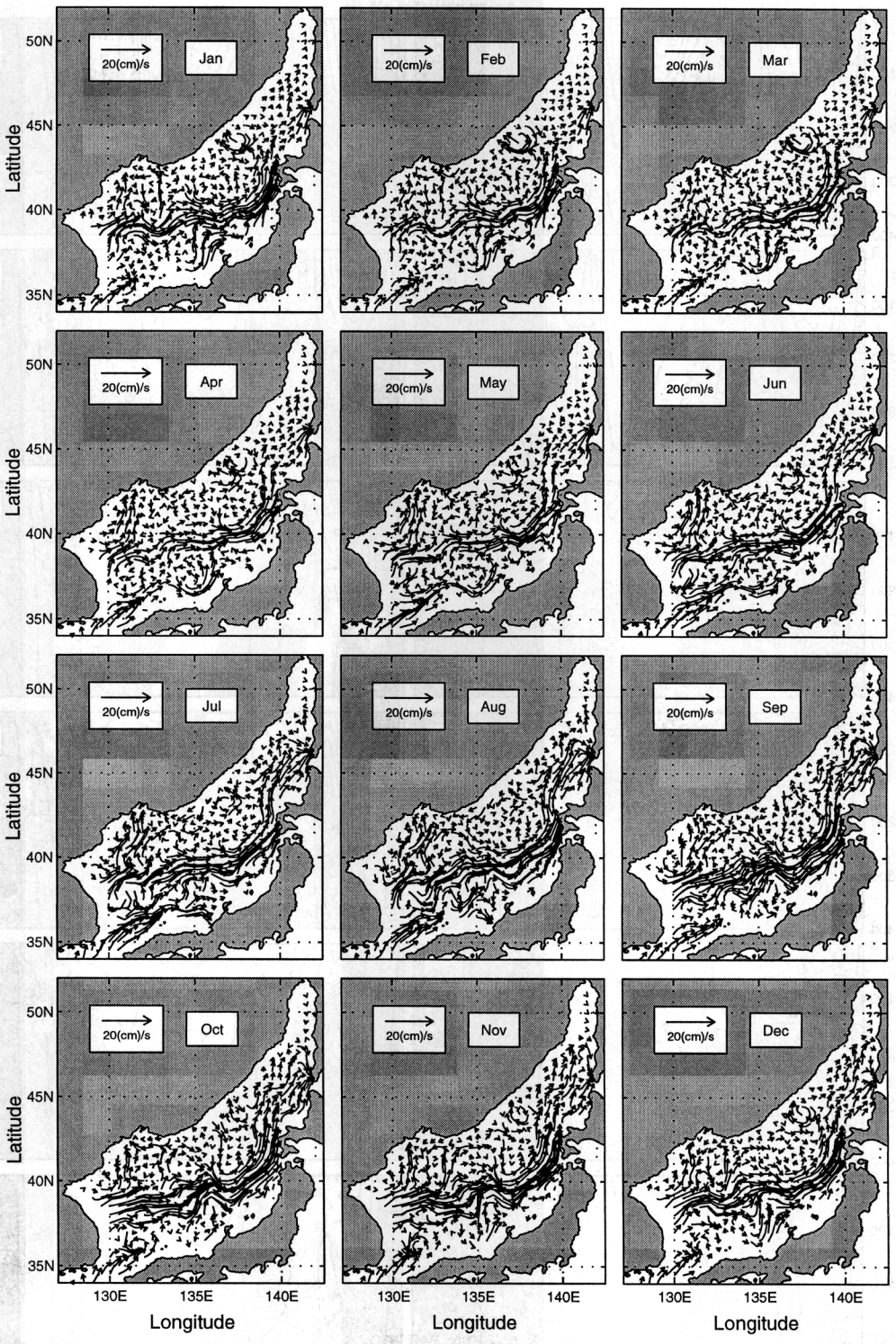

FIG. 6. Inverted monthly mean surface horizontal velocity vectors.

the variational P-vector method to invert the currents in shallow straits. The inverted general circulation pattern agrees with the observational circulation pattern using acoustic Doppler current profiler, reported by Egawa et al. (1993): The main axis of the TWC exists in the western channel at 34°N for all months, and the current in the eastern channel is relatively weak. The seasonal variation of the current magnitude is quite small. Northeastward steady flow always exists in the middle of the strait with a maximum current speed of 0.1 m s^{-1}.

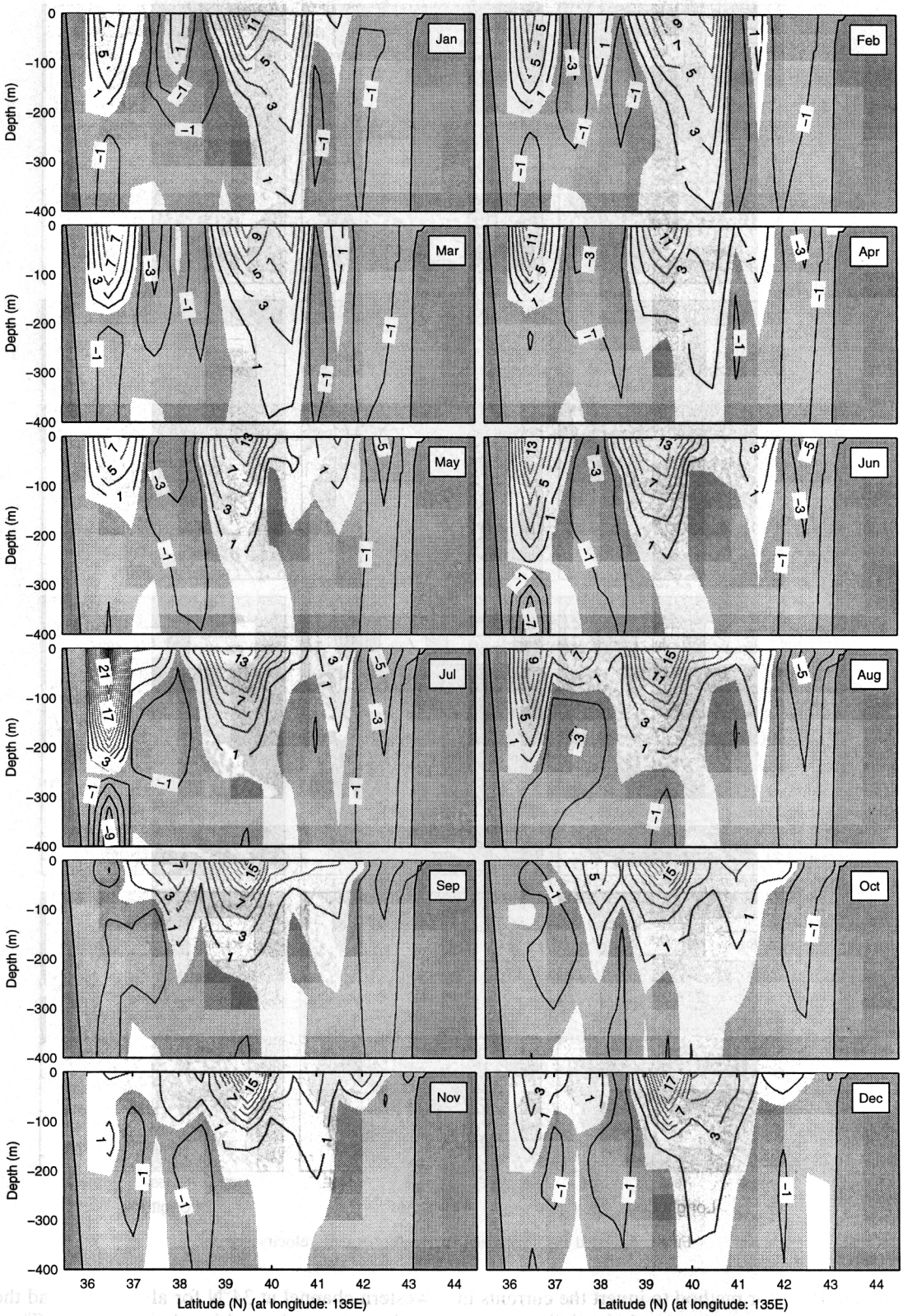

FIG. 7. Meridional cross-sections of the inverted monthly mean u velocity (cm s^{-1}) along 135°E.

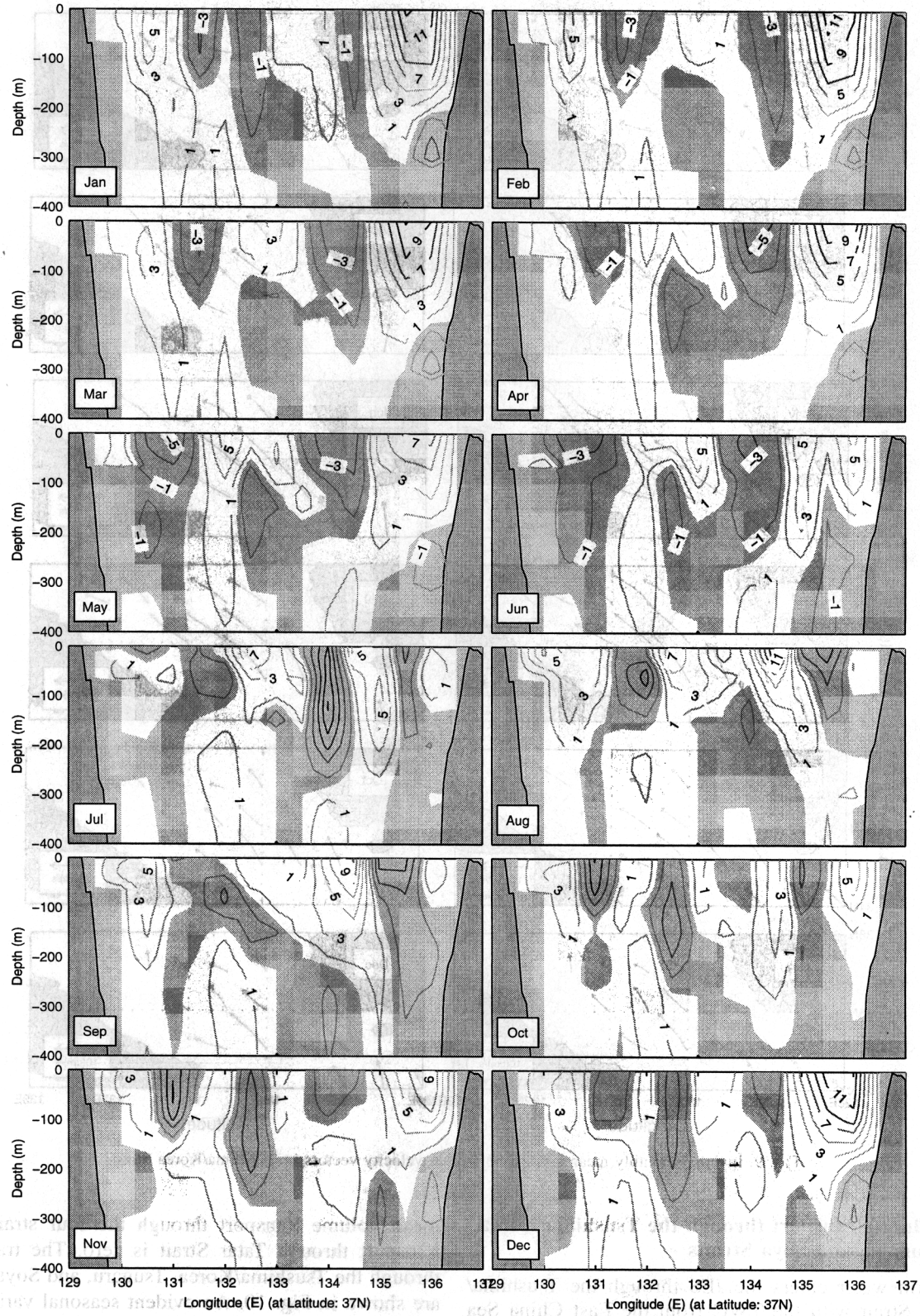

FIG. 8. Zonal cross-sections of the inverted monthly mean v velocity (cm s^{-1}) along 37°N.

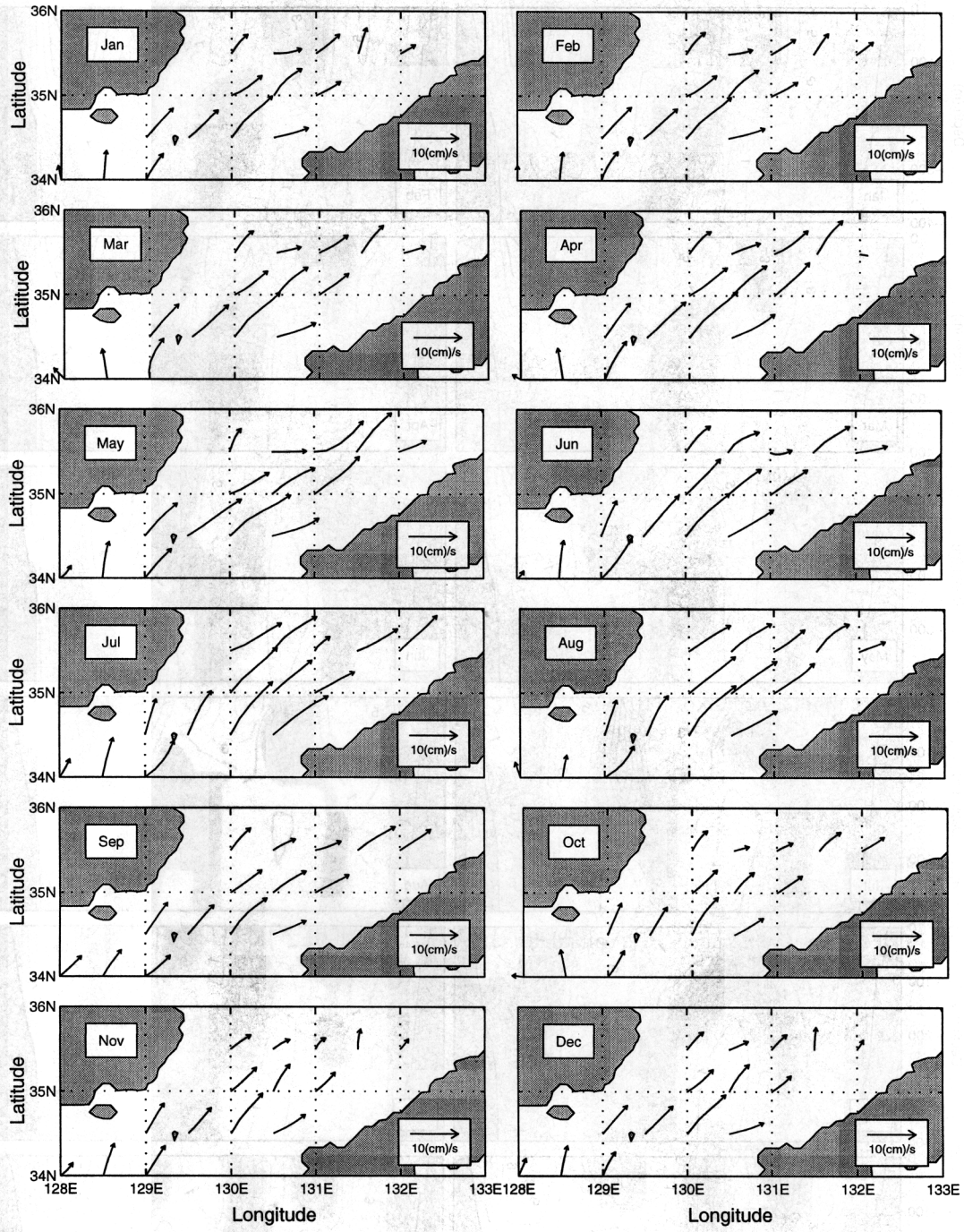

FIG. 9. Inverted monthly mean surface horizontal velocity vectors in Tsushima/Korea Strait.

6. Volume transport through the Tsushima/Korea, Tsugaru, and Soya Straits

Warm water enters the JES through the Tsushima/Korea Strait with the TWC from the East China Sea and exits the JES through the Tsugaru and Soya Straits. There is no evident volume transport through Tatar Strait (Martin and Kawase 1998). Using the inverted absolute geostrophic velocity field, we calculate the monthly mean volume transport through the four straits. The transport through Tatar Strait is zero. The transports through the Tsushima/Korea, Tsugaru, and Soya Straits are shown in Fig. 10. An evident seasonal variation is found in Tsushima/Korea Strait with a minimum value of 1.9 Sv in November and a maximum value of 2.9 Sv in July (Table 2.) The annual mean volume transport is 2.3 Sv, and the range (maximum minus minimum) of

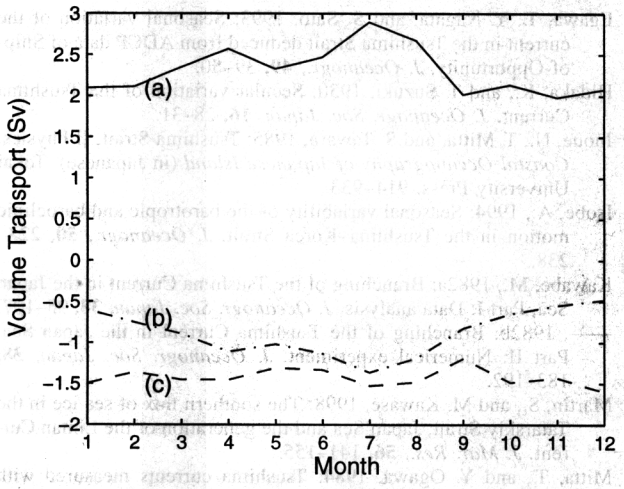

FIG. 10. Monthly mean volume transport through three major straits: Tsushima/Korea (a: solid), Soya (b: dot-dashed), and Tsugaru (c: dashed). Here positive (negative) values indicate inflow (outflow).

the seasonal variation is 1.0 Sv. This range (1.0 Sv) is larger than Isobe's (1994) estimation (0.7 Sv) using the sea level difference across the strait, and smaller than Inoue et al.'s (1985) estimation (1.61 Sv) with 3.43 Sv in summer and 1.82 Sv in winter, and Yi's (1966) estimation (1.9 Sv) with a maximum of 2.2 Sv in October, and a minimum of 0.3 Sv in February.

The volume transport in Soya Strait (outflow) has a similar seasonal variation to that in Tsushima/Korea Strait. The maximum (minimum) outflow from Soya Strait is 1.4 Sv (0.5 Sv) in July (December). The annual range is 0.9 Sv. The volume transport in Tsugaru Strait (outflow) has a rather weak seasonal variability. The maximum (minimum) outflow from Tsugaru Strait is 1.6 Sv (1.2 Sv) in December (September). The annual range is 0.4 Sv. The ratio of the outflow through Tsugaru versus Soya Strait varies from a maximum value of 3.2 in December to a minimum value of 1.1 in July.

Table 2 shows that the inverted inflow transport through Tsushima/Korea Strait equals the total outflow transport through Tsugaru and Soya Straits (a mass conservation pattern). Such a feature indicates the improvement of the variational P-vector method over the original P-vector method, and might be practically useful in determining open boundary conditions for regional numerical models. For example, some JES circulation models use constant outflow partitioning: Chu et al. (2001b) (or Bang et al. 1996) assumed that 75% (80%) of the total inflow transport flows out of the JES through Tsugaru Strait, and 25% (20%) through Soya Strait. Such an uncertainty in the open boundary conditions can be eliminated when the variational P-vector method is used.

7. Conclusions

The goal of this study is to investigate the seasonal variabilities of the Japan/East Sea circulation using the U.S. Navy's public domain Generalized Digital Environmental Model climatological hydrographic data and a recently developed variational P-vector method. The major results from this research are summarized as follows.

1) The variational P-vector method is a combined box/β-spiral model. It has shown the capability to invert the Japan/East Sea circulation reasonably well, and in particular at the three major straits: Tsushima/Korea, Tsugaru, and Soya Straits. The inverted absolute geostrophic velocity field coincides with earlier observational depiction of the Japan/East Sea circulation.
2) We estimate the monthly mean transport through three major straits: Tsushima/Korea, Tsugaru, and Soya Straits. The volume transports through the Tsushima/Korea and Soya Straits have evident seasonal variabilities. The annual mean volume transport through the Tsushima/Korea Strait is 2.3 Sv with the maximum (minimum) inflow of 2.9 (1.9) Sv in July (November). The annual mean volume transport through the Soya Strait is 0.9 Sv with the maximum (minimum) outflow of 1.4 (0.5) Sv in July (December). The volume transport through the Tsugaru Strait (outflow) has a rather weak seasonal variability. The maximum (minimum) outflow from the Tsugaru Strait is 1.6 (1.2) Sv in December (September).
3) The major feature of the inverted annual mean circulation is the three-branch structure in the upper layer (surface to 100 m) and the multieddy structure in the intermediate layer (100 to 300 m). In the upper layer, the Tsushima Warm Current bifurcates north of 35°N into the eastern portion [Japan nearshore branch i.e., the first branch] and a western portion [the East Korean Warm Current]. The East Korean Warm Current moves northward and separates near 37°–38°N into two branches: the offshore branch (the second branch) follows the Subpolar Front to the western coast of Hokkaido Island, and the longshore branch (or the third branch), moves northward. This three-branch pattern weakens with depth. In the intermediate layer, an evident cyclonic gyre is identified in the Japan Basin (JB; 38°–44°N, 135°–140°E) with the flow associating with the second branch as its southern and eastern flanks and the flow from the north as its western flank. The maximum swirl speed of this gyre is around 0.1 m s^{-1}. A mesoscale anticyclonic eddy is identified in the Ulleng/Tsushima Basin (36°–38°N, 130°–132°E) with a maximum swirl speed of 0.06 m s^{-1}. This mesoscale anticyclonic eddy weakens with depth.
4) An out-of-phase variability is found between two major eastward currents: the Japan nearshore branch, and the Tsushima Warm Current along the subpolar Front. During the prevailing summer monsoon season (Jun–Oct), the Tsushima Warm Current along the subpolar Front strengthens with the maximum speed increasing from 0.12 to 0.18 m s^{-1}, and the

Japan Nearshore Branch weakens with the maximum speed decreasing from 0.12 to 0.04 m s^{-1}. During the prevailing winter monsoon season (Dec–Apr), the Tsushima Warm Current along the Subpolar Front weakens with the maximum speed decreasing from 0.18 to 0.12 m s^{-1}, and the Japan nearshore branch strengthens with the maximum speed increasing from 0.04 to 0.12 m s^{-1}.

5) The mesoscale anticyclonic eddy in the Ulleng/Tsushima Basin has seasonal variability. The eddy is quite evident during the whole winter season (Dec–Feb) and weakens in March. It cannot be identified at the 37°N cross-section from spring to early summer (Apr–Jun) and appears again in late summer (Aug).
6) Currently, the JES numerical models are generally initialized with either observed or climatological temperature and salinity, as well as zero velocity. This leads to an imbalance between the density and velocity fields during the spinup period. The Navy's GDEM *T, S* and the inverted velocity fields provide balanced initial fields for Japan/East Sea numerical modeling and simulation.

Acknowledgments. This work was funded by the Office of Naval Research (N0001401WR20218), the Naval Oceanographic Office, and the Naval Postgraduate School.

REFERENCES

Bang, I., J.-K. Choi, L. Kantha, C. Horton, M. Cliford, M.-S. Suk, K.-I. Chang, S. Y. Nam, and H.-J. Lie, 1996: A hindcast experiment in the East Sea (Sea of Japan). *La mer,* **34,** 108–130.

Chu, P. C., 1995: P-vector method for determining absolute velocity from hydrographic data. *Mar. Technol. Soc. J.,* **29** (3), 3–14.

——, 2000: P-vector spirals and determination of absolute velocity. *J. Oceanogr.,* **56,** 591–599.

——, C. R. Fralick, S. D. Haeger, and M. J. Carron, 1997a: A parametric model for Yellow Sea thermal variability. *J. Geophys. Res.,* **102,** 10 499–10 508.

——, S. K. Wells, S. D. Haeger, C. Szczechowski, and M. Carron, 1997b: Temporal and spatial scales of the Yellow Sea thermal variability. *J. Geophys. Res.,* **102,** 5655–5668.

——, C. W. Fan, and W. J. Cai, 1998a: Evaluation of P-vector method using modular ocean model (MOM). *J. Oceanogr.,* **54,** 185–198.

——, ——, C. J. Lozano, and J. L. Kerling, 1998b: An airborne expandable bathythermograph survey of the South China Sea, May 1995. *J. Geophys. Res.,* **103,** 21 637–21 652.

——, J. Lan, and C. W. Fan, 2001a: Japan Sea thermohaline structure and circulation. Part I: Climatology. *J. Phys. Oceanogr.,* **31,** 244–271.

——, S. H. Lu, C. W. Fan, and C.-S. Kim, 2001b: Modeling of Japan Sea circulation and thermohaline structure. *Advances in Coastal Modeling,* V. C. Lakhan, Ed., Elsevier Science, in press.

Egawa, T., Y. Nagata, and S. Sato, 1993: Seasonal variation of the current in the Tsushima Strait deduced from ADCP data of Ship-of-Opportunity. *J. Oceanogr.,* **49,** 39–50.

Hidaka, K., and T. Suzuki, 1950: Secular variation of the Tsushima Current. *J. Oceanogr. Soc. Japan,* **16,** 28–31.

Inoue, N., T. Mitta, and S. Tawara, 1985: Tsushima Strait, II Physics. *Coastal Oceanography of Japanese Island* (in Japanese). Tokai University Press, 914–933.

Isobe, A., 1994: Seasonal variability of the barotropic and baroclinic motion in the Tsushima–Korea Strait. *J. Oceanogr.,* **50,** 223–238.

Kawabe, M., 1982a: Branching of the Tsushima Current in the Japan Sea, Part I: Data analysis. *J. Oceanogr. Soc. Japan,* **38,** 95–107.

——, 1982b: Branching of the Tsushima Current in the Japan Sea, Part II: Numerical experiment. *J. Oceanogr. Soc. Japan,* **38,** 183–192.

Martin, S., and M. Kawase, 1998: The southern flux of sea ice in the Tatarskiy Strait, Japan Sea and the generation of the Liman Current. *J. Mar. Res.,* **56,** 141–155.

Mitta, T., and Y. Ogawa, 1984: Tsushima currents measured with current meters and drifters. *Ocean Hydrodynamics of the Japan and East China Seas,* T. Ichiye, Ed., Elsevier Science, 67–76.

Moriyasu, S., 1972: The Tsushima current. *Kuroshio, Its Physical Aspects,* H. Stommel and K. Yoshida, Eds., University of Tokyo Press, 353–369.

Press, W. H., B. P. Flannery, S. A. Teukolsky, and W. T. Vetterling, 1986: *Numerical Recipes—The Art of Scientific Computing.* Cambridge University Press, 660–667.

Seung, Y. H., 1992: A simple model for separation of East Korean Warm Current and formation of the North Korean Cold Current. *J. Oceanol. Soc. Korea,* **27,** 189–196.

——, and J.-H. Yoon, 1995: Some features of winter convection in the Japan Sea. *J. Oceanogr.,* **51,** 61–73.

Stommel, H., and F. Schott, 1977: The beta spiral and the determination of the absolute velocity field from hydrographic station data. *Deep-Sea Res.,* **24,** 325–329.

Suda, K., and K. Hidaka, 1932: The results of the oceanographic observations on board R.M.S. 'Syunpu Maru' in the southern part of the Japan Sea in the summer of 1930 (in Japanese). *J. Oceanogr. Imp. Mar. Observ.,* **4,** 1–174.

——, K. Hidaka, Y. Matsudaira, E. Kurashige, H. Kawasaki, and T. Kubo, 1932: The results of the oceanographic observations on board R.M.S. 'Syunpu Maru' in the southern part of the Japan Sea in the summer of 1929, Part I (in Japanese). *J. Oceanogr. Imp. Mar. Observ.,* **3,** 291–375.

Teague, W. J., M. J. Carron, and P. J. Hogan, 1990: A comparison between the Generalized Digital Environmental Model and Levitus climatologies. *J. Geophys. Res.,* **95,** 7167–7183.

Toba, Y., K. Tomizawa, Y. Kurasawa, and K. Hanawa, 1982: Seasonal and year-to-year variability of the Tsushima–Tsugaru Warm Current system with its possible cause. *La mer,* **20,** 41–51.

Uda, M., 1934: The results of simultaneous oceanographic investigations in the Japan Sea and its adjacent waters in May and June (in Japanese). *J. Imp. Fish. Exp. Sta.,* **5,** 57–190.

Wunsch, C., and B. Grant, 1982: Towards the general circulation of the North Atlantic Ocean. *Progress in Oceanography,* Vol. 11, Pergamon, 1–59.

Yi, S. U., 1966: Seasonal and secular variations of the water volume transport across the Korea Strait. *J. Oceanol. Soc. Korea,* **1,** 7–13.

Yoon, J.-H., 1982: Numerical experiment on the circulation in the Japan Sea Part, III. Mechanism of the Nearshore Branch of the Tsushima Current. *J. Oceanogr. Soc. Japan,* **38,** 125–130.